Supplementary information file

Lattice Strain Induced *d*-band Centre Engineering Enabled Pseudocapacitive Energy Storage in 2D Hypo-Hyper Electronic V-$NiCo_2O_4$ for Asymmetric Supercapacitors

Soumyajit Maitra[1], Krishnendu Roy[1], Dibyendu Ghosh[1], and Praveen Kumar[1*]

[1]*School of Materials Science, Indian Association for the Cultivation of Science, Kolkata 700032, India.*

**Corresponding Author Email: praveen.kumar@iacs.res.in*

Experimental Section

Materials

Carbon Cloth (Sigma), Cellulose paper (Sigma), Potassium Hydroxide (Sigma), Nickel Nitrate hexahydrate (Sigma) Cobalt Nitrate hexahydrate (Sigma) Ammonium Metavanadate (Sigma) Diethyl triamine penta-acetic acid (DTPA) (Merck), Urea (Fisher), Nitric Acid (Merck), Sulfuric Acid (Merck), Naphthalene (Sigma), D-Glucose (Sigma), DI Water (Merck) Ethanol (Merck), polyvinylidene fluoride (PVDF) (Sigma), N-Methyl pyrrolidone (NMP) (Sigma)

Fabrication of pristine and V-doped $NiCo_2O_4$ electrode

Prior to the fabrication of the electrodes, the purchased carbon cloth was thoroughly cleaned by sonication in DI water followed by functionalization by immersing in a hot solution of 1:3 volumetric ratio of HNO_3 and H_2SO_4 at 90°C for 6 hours. The carbon cloth, post-treatment, was rinsed multiple times with DI water until pH of rinsed water was observed to be 7 indicating removal of functionalization acid. In a 100 ml beaker, 40 ml DI water was added along with the addition of 0.01M $Ni(NO_3)_2.6H_2O$, 0.02 M $Co(NO_3)_2.6H_2O$, and 0.09M Urea, and 0.03M DTPA followed by constant stirring. Ammonium metavanadate was added as the V source resulting in solutions with 0, 1, 3, and 5 mol % Vanadium vs Ni concentration followed by stirring until complete dissolution of the reagents. The pristine solution without vanadium first turned pink followed by a color change to purple indicating complexation with DTPA. With subsequent vanadium incorporation, an initial yellow tinge was observed which is characteristic color of the VO_2^+ chelation complex followed by a gradual change of solution color to greenish blue. After clear solutions devoid of any undissolved particulates were observed, the solution was poured into a Teflon-lined stainless-steel autoclave with the cleaned and functionalized carbon cloth placed inside. The autoclaves were placed inside the furnace followed by heating at 145°C for 16 hours. After completion of the reaction, the carbon cloths were taken out, rinsed with water and ethanol, and dried under a vacuum. A critical observation at this point was the color of the deposited films on carbon cloth. The pristine sample has a

light translucent pink coating while V-doped samples have a light yellowish-brown color. However, after annealing at 450℃ for 2 hours, all the films turned black in color. The precipitated powder at the bottom of the Teflon containers was centrifuged, purified, annealed, and stored for further analysis. The samples with V doping 0%, 1%, 3%, and 5% were labeled as NCV0, NCV1, NCV3, and NCV5 respectively.

Fabrication of functionalized carbon nanosphere electrode

Carbon nanospheres (CNs) were also synthesized also by a one-step hydrothermal method followed by functionalization. As described previously, 0.5 mol/L of glucose solution was placed in the hydrothermal reactor at 190℃ for 6 hours. The obtained black precipitate was collected, centrifuged, and washed thoroughly with water and ethanol followed by drying. Functionalization was again carried out in an oxidizing acid bath comprising 2 M HNO_3 in which the CNs were sonicated for 30 minutes followed by heating at 90℃ for another 30 mins. The functionalized sample was then collected and dried. 50 mg of the obtained nanospheres were taken followed by the addition of 10 mg PVDF as a binder and 5 ml NMP. The mixture was sonicated for 4 hours till a black homogeneous uniform dispersion was obtained. The solution was drop-cast onto the functionalized carbon cloth followed by drying under infra-red light. The mass loading was controlled by drop-casted solution volume and was repeated in cycles till adequate mass loading was observed.

Assembly of asymmetric hybrid supercapacitor Material Characterization

Supercapacitor device assembly was carried out using standard protocols described previously. In a typical assembly process, the specific capacitance value of the positive electrode (C_{s+}) and the negative electrode (C_{s-}). Based on the concept of charge balance, we use the following equation[1,2]

$$\frac{m_+}{m_-} = \frac{C_{s+}}{C_{s-}} \times \frac{\Delta U_+}{\Delta U_-} \quad \ldots (S1)$$

3M KOH solution was prepared and a cleaned piece of cellulose paper was taken. The electrodeposited positive electrode and the CNs negative electrode were soaked in KOH followed by pressing to form a sandwich configuration with KOH-soaked Cellulose paper separator in the middle. A length of 1 cm of bare carbon was exposed at either end from where the contact was taken and attached to the external load. Here in equation (1) m+ and m− represent the mass of positive electrode and negative electrode, ΔU+ and ΔU− stand for the potential window within which the CV for the corresponding positive and negative electrodes.

Material Characterization

X-Ray diffraction calculations were carried out using Rigaku SmartLab X-Ray diffractometer with Cu-Kα (λ = 1.541 Å) as the source. Field emission gun scanning electron microscopy (FESEM) (JEOL JSM-7500F) was used with field emission gun transmission electron microscopy (JEOL, JEM 2100F) with built in Energy dispersive X-Ray Spectra (EDAX) for elemental mapping using Oxford Inca System. Raman spectroscopy was carried out with Horiba T64000 Raman spectrometer with 488 nm laser excitation was used. Brunauer-Emmett-Teller (BET) isotherms were measured using N_2 adsorption desorption experiments at 77 K using Quantachrome Autosorb iQ. XPS spectra were measured using Physical Electronics 5400 ESCA instrument. AFM was carried out by using 1a Multimode V 7.0 AFM (Veeco, Santa Barbara, CA). Fourier Transform Infra-Red (FTIR) Spectra was analyzed using a PerkinElmer TV1900 FTIR spectrometer (Waltham, MA).

XRD Measurements

XRD measurements were used to elucidate crystal structure and morphology of the prepared samples for understanding the effect of doping of lattice strain [3,4]

$$\lambda = 2d_{hkl}sin\theta_{hkl} \quad \ldots(S2)$$

$$\frac{1}{d_{hkl}^2} = \frac{h^2 + k^2 + l^2}{a^2} \quad \ldots(S3)$$

$$\beta_{hkl} = \frac{K\lambda}{D} + 4\varepsilon \times sin\theta_{hkl} \quad \ldots(S4)$$

$$\delta = \frac{1}{D^2} \quad \ldots(S5)$$

$$\langle \varepsilon_{rms(hkl)} \rangle = \left(\frac{2}{\pi}\right)^{0.5} \times \frac{\Delta d_{hkl}}{d_{hkl}} \quad \ldots(S6)$$

Here λ indicates wavelength of incident X-Rays, d_{hkl} refers to the d spacing of <hkl> family of planes θ is Braggs Angle, a is lattice constant for cubic crystal, β is FWHM of XRD peaks, K is a constant equal to 0.9, D is crystallite size, ε is microstrain, δ is dislocation density, $\langle \varepsilon_{rms(hkl)} \rangle$ is the root mean squared strain. Equation (4) is used for the Williamson - Hall plot.

Table S1. Crystallographic data obtained from XRD measurements

Sample	D-spacing <d> (Å)	a (Å)	Dislocation density (δ)	Crystallite Size (D) (nm)	Microstrain (ε)	RMS Strain (ε_{rms})
NCV0	25.7	8.121	1.04E-3	31	1.66E-3	1.56E-3
NCV1	24.9	8.011	1.37E-3	27	2.47E-3	1.51E-2
NCV3	23.4	7.93	1.89E-3	23	2.79E-3	2.19E-3
NCV5	22.03	7.78	2.77E-3	19	3.03E-3	2.78E-3

Electrochemical Analysis

Electrochemical analysis was carried out using an electrochemical workstation (Bio-Logic Science Instruments, Model SP-300/ 240). The electrodes were individually analyzed using a three-electrode configuration using an SCE reference electrode and graphite rod as the counter electrode. Cyclic Voltammetry (CV) and Galvanic Charge Discharge (GCD) techniques were employed to understand electrochemical charge storage whereby 3 M KOH was used in all experiments. EIS measurements were carried out using from 10 mHz to 1MHz at 5 mV Vs SCE. Device testing was carried out using a 2-electrode-setup[5–7].

$$C_{sCV} = \frac{\oint_{V1}^{V2} idV}{2\vartheta\Delta V} \quad \text{…(S7)}$$

$$C_{sGCD} = \frac{I \times \Delta t}{\Delta V} \quad \text{…(S8)}$$

$$\eta\% = \frac{t_{discharge}}{t_{charge}} \times 100 \quad \text{…(S9)}$$

$$E = \frac{1}{2} C_s V^2 \quad \text{…(S10)}$$

$$P = 3600E/t \quad \text{…(S11)}$$

Where C_{sCV} is the specific capacitance obtained from the CV plots, C_{sGCD} is the specific capacitance obtained from the GCD plots, V_1 an V_2 represents the CV potential window, and ν is the CV scan rate. Δt is the discharge time for GCD through the potential range of ΔV. η% is Coulombic efficiency, Δt_{charge} and $\Delta t_{discharge}$ are the time required for full charge and discharge respectively of the supercapacitor device as well as electrodes. E is energy density (W hr/Kg) and P is Power density (W/Kg).

Ragone Plots of the fabricated supercapacitor devices have been compared with similar $NiCo_2O_4$ based materials from recent reports[8–17] and have been presented in Fig S6.

Computational Details

DFT calculations were carried out using CASTEP code using $9 \times 9 \times 3$ k-point grid according to the Monkhorst-Pack scheme. The functional used in the simulations were of Perdew-Burke-Erzenhof (PBE) form with pseudopotential being of Ultrasoft type and Koelling-Hammon relativistic treatment with Pulay type Density Mixing Scheme[18–20]. The plane wave basis set cut-off was set at 1320 eV. SCF threshold was set at 1×10^{-6} eV[20–22]. Hubbard corrections were included in calculations to account for electronic localizations and self-interaction. GGA+U exchange-correlation (XC) were used during the simulation process, where the U value for d orbitals of Ni d was set at 5 eV, Co was set at 4.5, and V was set at 3.4 eV. Geometry optimizations were carried out using the LBFGS algorithm along with optimization of the structure after every cycle with a max displacement of 0.001 Å, max stress set at 0.01 GPa, and energy cutoff set at $1x10^{-6}$ eV. The slab models were created by placing a (311) facet slab model 4.36 Å thick layer of optimized V-doped $NiCo_2O_4$. A vacuum length of 30 Å was kept to prevent interlayer interactions. Self-consistent Dipole slab corrections were implemented to reduce any interlayer interaction. The diffusion of OH- ions through the adsorbed water layer to the surface of the oxide slab has been investigated using a series of methods. At first water surface coverage and stability of the number of OH- ions over the slab model were verified using structural relaxation. Then, Monte Carlo simulations along with AIMD were employed to observe the orientation of the water molecules and the OH- ion over the preferred sites on the slab[23–25]. From this model, a diffusion barrier simulation was carried out to understand the path with least activation energy for hydrated OH- to approach and stabilize on the slab surface. Next transition state kinetics using complete linear synchronous transit/quadratic synchronous transit (LST/QST) search for locating and optimizing transition state using NEB ensemble were carried out to understand the methodology of the progress of the pseudocapacitive reaction mechanism leading to the reactive intermediates resulting in charge storage[26]. At first a 2 x 2 x 1 (311) facet slab model 4.36 Å thick was taken followed by adjusting a vacuum level of 30 Å. At first, the surface coverage of the slab with water molecules and OH- ions was scanned to ensure a stable double-layer coverage using structural relaxation according to previous methods. Sorption code was used to adsorb the adsorbing species on the adsorbent using a fixed loading method with Metropolis method at 298 K using Dreiding Forcefield and Ewald Summation method. Structural relaxation was carried out to optimize the adsorbed structures. Several ratios of H_2O: OH- were taken and a ratio of 6:1 was found to be structurally most stable. The geometric arrangement was further stabilized with 2 picoseconds of AIMD simulations using NVT ensemble with a constant temperature of

293 K using Nose Thermostat using Nose Q ratio equal to 1 and XL-BOMBD extended Lagrangian[27,28]. For all simulations, DFT+U level of theory was used. After stabilization of the initial orientation of the water molecules and the OH- ion on the surface of the slab diffusion pathway of hydrated OH- ions followed by surface reaction pathways were calculated according to previous reports using Cl-NEB methods implementing LST/QST search method for finding the transition state. RMS convergence of 0.01 eV/ Å was used with optimization of reactants and products in each step to extract vibrational frequencies later required for zero-point energy (ZPE) calculations[29,30]. The ΔG calculations for the reactions were modeled from OER since the use of OH- ions on a hydrated oxide surface of since the initial stages of pseudocapacitive charge storage are similar to OER without progression to O_2 evolution where the OH- ion diffuses onto the surface of the slab and attaches to the catalytically active favorable metal site (O-M*) to for a MOOH adduct followed by stabilization of geometry of the OH- and the double layer water molecules. It is a one-step adduct formation and the stabilization of the complex has been explored in 4 more steps using DFT-D3 corrections to take into consideration H-bonding[27,31,32].

$$\Delta G = E\ (Slab + n\ H_2O + m\ OH\text{-}) - E\ (Slab) - m\ E\ (OH\text{-}) - n\ E\ (H_2O) + \Delta ZPE - T\Delta S + k_B T ln10 \times pH \quad \ldots(S12)$$

$$\Delta G = \Delta E_i - \Delta E_j + \Delta ZPE_{i-j} - T\Delta S_{i-j} + k_B T ln10 \times pH \quad \ldots(S13)$$

Here ΔG represents the Gibbs Free energy. The first term in the equation on the right represents the Enthalpy of the slab with the electrolyte layer containing n H2O molecules and m OH- molecules, the second term represents the Enthalpy of the empty slab, the 4th and 5th terms show the enthalpy values of the water molecules and OH- ions respectively while ZPE represents Zero Point Energy, T is the temperature in Kelvin and ΔS is the change in entropy. The ZPE values are calculated from the equation[31,32]

$$ZPE = \frac{1}{2}\Sigma_i h\vartheta_i \quad \ldots(S14)$$

Where ZPE is sum of all the vibrational frequency modes obtained from the geometry optimization of the reactant product and intermediate states in the LST/QST transition state search. The entropy change for water here is obtained from NIST tables. In equation (2) the ΔE_i and ΔE_j represent the Enthalpy change between the ith and jth steps for optimization of the M-OH hydrated intermediate at the surface. The diffusion of hydrated OH- ions over the oxide surface was also used carried out using the same approach using the Cl-NEB ensemble as described previously for ion diffusion in batteries for energy storage

Quantum Capacitance calculations were calculated according to previous reports[33–35].

$$\Delta Q = \int_{-\infty}^{+\infty} D(E)[f(E) - f(E - e\phi_G)]\, dE \quad \ldots(S15)$$

$$C_Q = e^2 \int_{-\infty}^{+\infty} D(E)[F_T(E - e\phi_G) dE \quad \ldots(S16)$$

Where, $F_T(E) = (4k_B\mathrm{T})\ sech^2(\mathrm{E}/2k_BT)$

$$Q = \int_0^{\phi_G} C_Q D\varphi \quad \ldots(S17)$$

Here, ΔQ refers to the excess charge density, D(E) is the density of states, f(E) is the Fermi Dirac statistics distribution function, E is the energy with reference to the Fermi level, e is the elementary electric charge k_B is Boltzmann's constant, $F_T(E)$ is the thermal broadening function, C_Q is quantum capacitance and Q is stored surface charge[36–38]

Formation energy calculations have been carried out using previous reports[19,32,39].

V doping was performed at both the Ni site and Co site to check the favourability of the substitution.

$$\Delta E_F = \Delta E_{V-NiCo_2O_4} - \Delta E_{NiCo_2O_4} - \mu_{Ni} + \mu_V \quad \ldots(S18)$$

for V substitution at the Ni site and

$$\Delta E_F = \Delta E_{V-NiCo_2O_4} - \Delta E_{NiCo_2O_4} - \mu_{Co} + \mu_V \quad \ldots(S19)$$

for V substitution at the Co site.

Where ΔE_F is the formation energy, $\Delta E_{V-NiCo_2O_4}$ is the enthalpy of V doped NiCo2O4, $\Delta E_{NiCo_2O_4}$ is the enthalpy of Pristine NiCo2O4, μ_{Ni} is the chemical potential of Ni, μ_{Co} is the chemical potential of Co and μ_V is the chemical potential of V.

The chemical potentials for Ni and Co were obtained from geometry optimized unit cells of NiO and Co_3O_4. The chemical potential of O was obtained from molecular O_2. Here V was a dopant and the reaction was carried out in O rich environment containing Ni and Co. so the chemical potential μ_V was derived from pristine V_2O_5 as opposed to metallic V.

The obtained ΔE_F change for V substitution in Ni site was found to be -7.69 eV while for Co site it was -5.33 eV. Hence it can be concluded that V doping in the Ni site is more favorable compared to Co site.

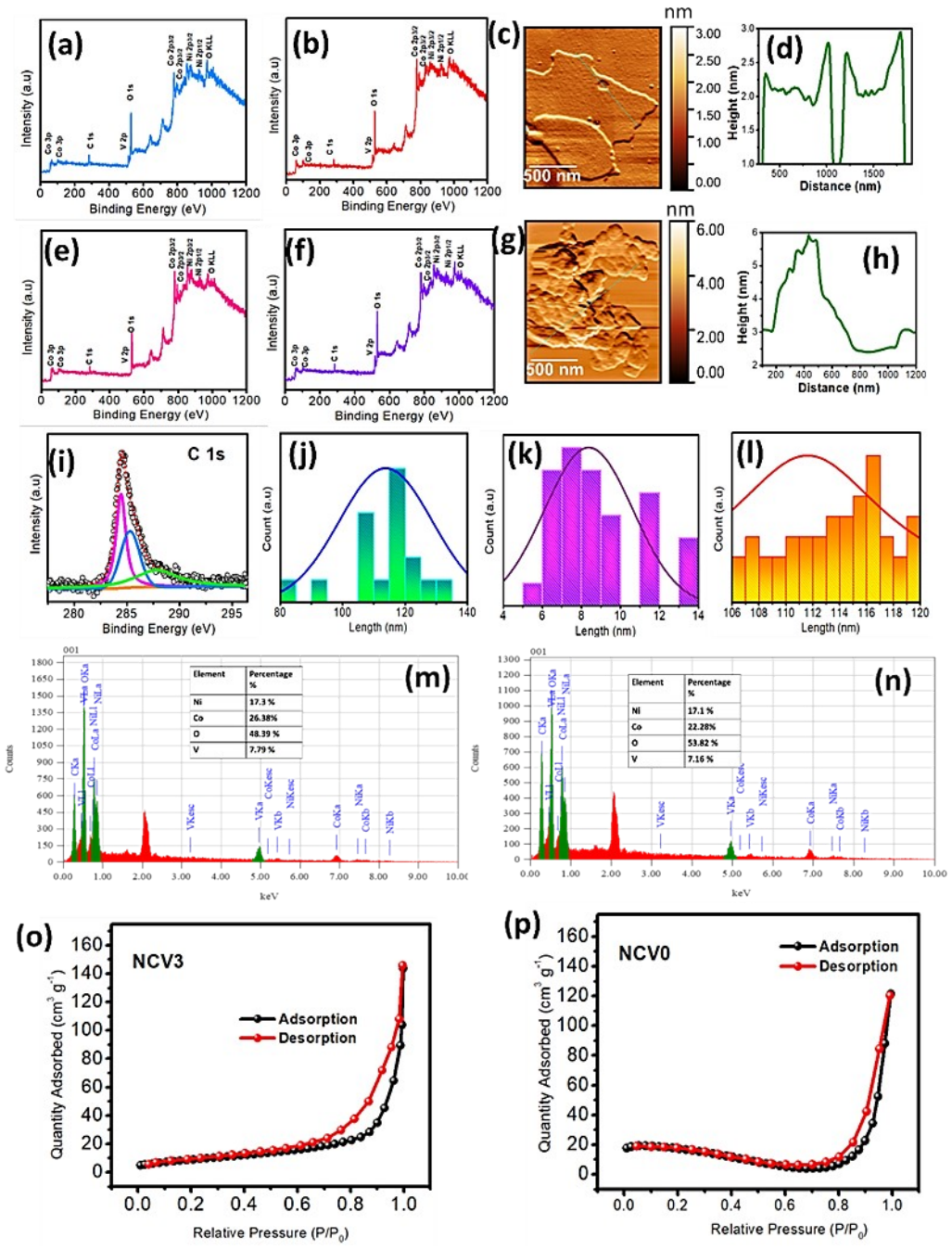

Fig S1. XPS full survey spectrum of (a) NCV3 (b) NCV1 and (e) NCV0 (f) NCV5 (c) AFM image of NCV0 nanosheet with (d) line profile of NCV0 (g) AFM image of NCV3 wrinkled nano-bundle with (d) line profile of NCV3 (i) XPS C1s core level of functionalized blank carbon cloth (j) Size distribution plot of inter-nanosheet pore gap in NCV0 (k) Size distribution plot of nanosheet thickness of NCV3 wrinkled bundles (l) Size distribution plot of inter-nanosheet pore gap in NCV3 (m) EDX plots of NCV3 after stability test (n) EDX plots of NCV3 after synthesis. (o) BET adsorption isotherm of NCV3 (p) BET adsorption isotherm of sample NCV0

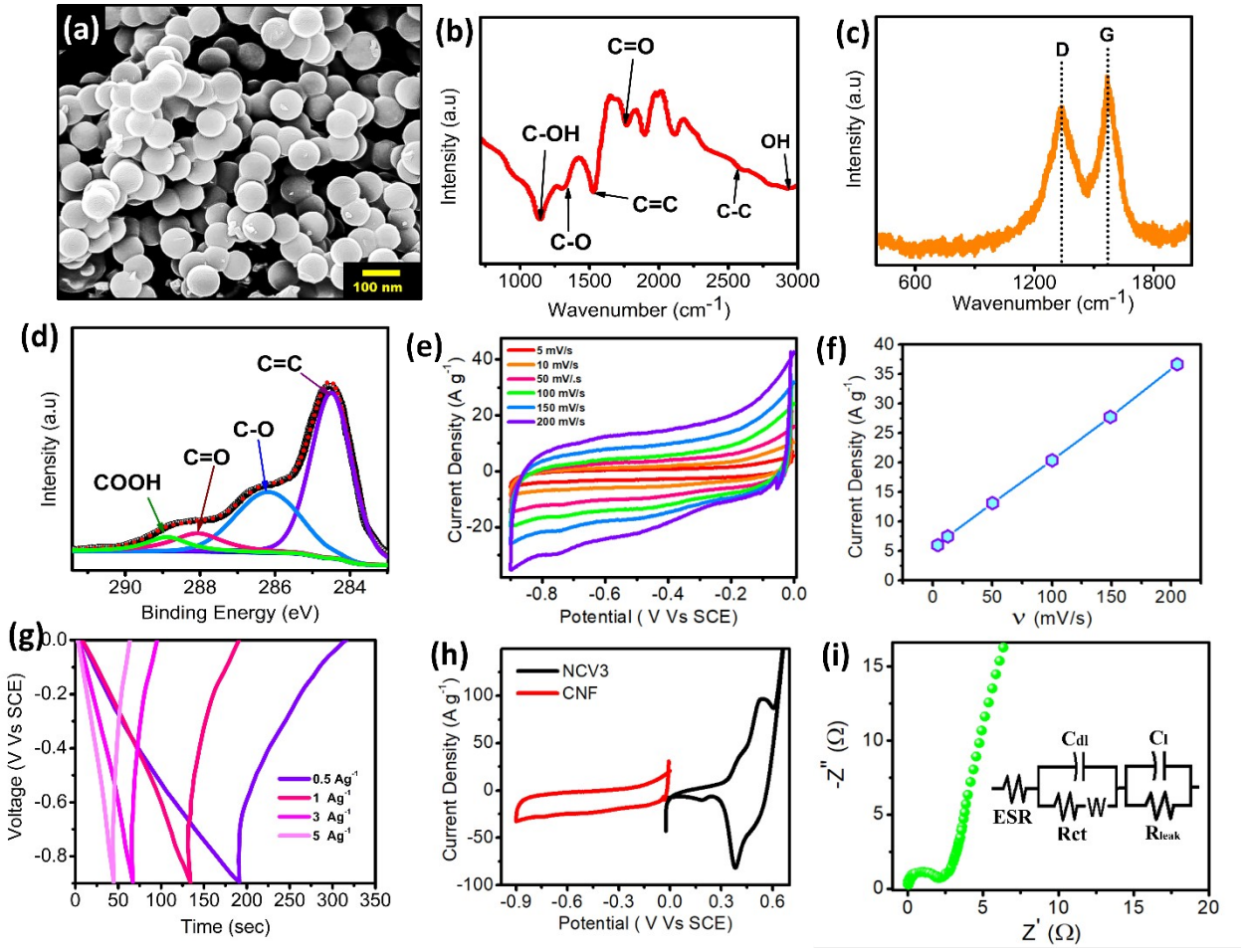

Fig S2. (a) SEM image of functionalized carbon nanospheres (CNS) (b) FTIR spectrum of CNS (c) Raman spectrum of CNS (d) XPS C 1s core level of CNS (e) CV plots of CNS negative electrode are varying scan rates (f) plot of peak current density vs scan rate (g) GCD plots of CNS negative electrode are varying current densities (h) Overlay of CV plot of CNS and NCV3 at 25 mVs^{-1} (i) EIS plot of CNS with Randle's circuit in the inset

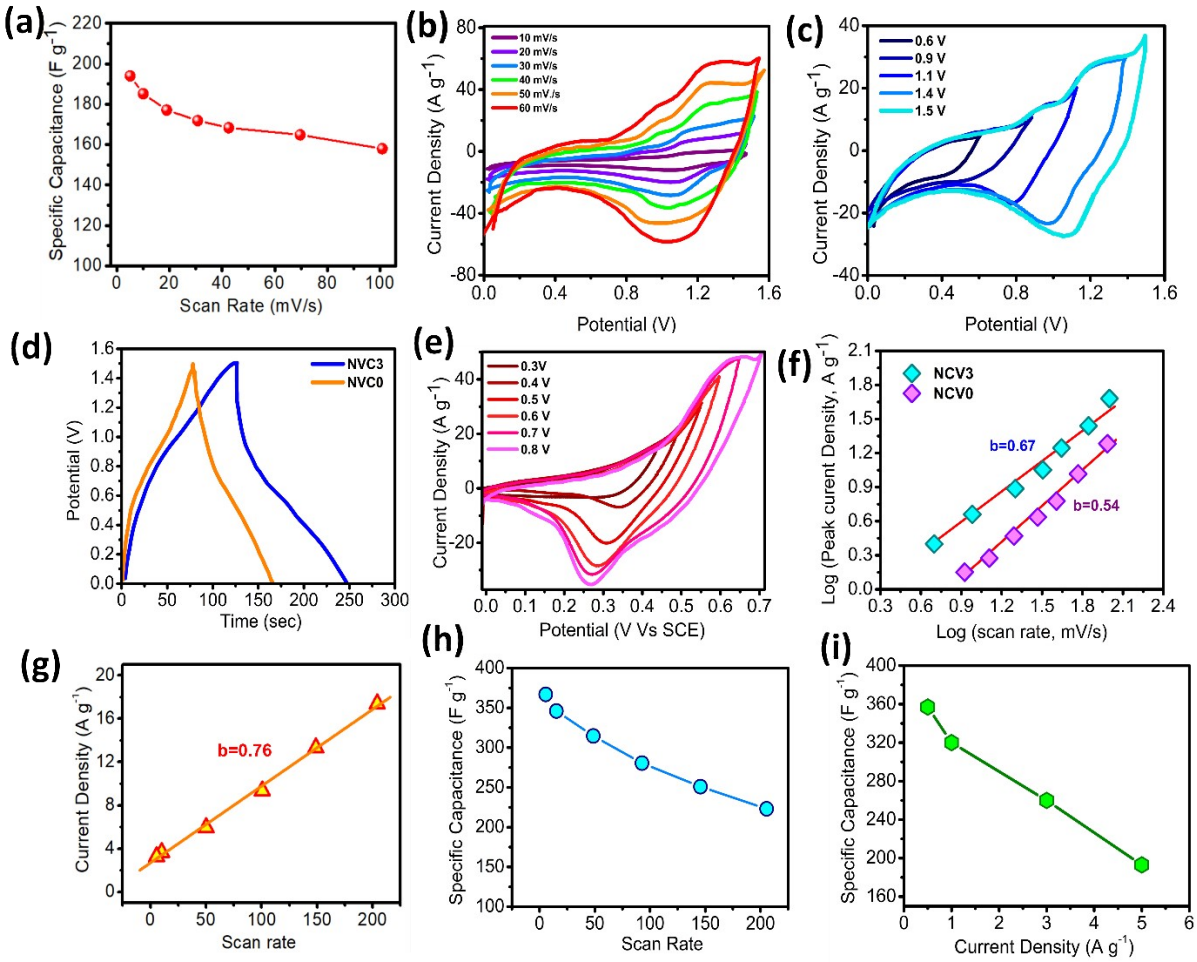

Fig S3. (a) Plot of Capacitance Vs scan rate of NCV3-PC (b) CV plots at various scan rates of NCV3-PC (c) CV plots of NCV3-PC at various operating voltage values (d) Overlay of GCD plot of PC devices (e) CV plot of NCV0 electrode in 3 electrode configuration at various operating voltage values (f) Log plot of Peak current and scan rate of NCV3 and NCV0 (g) Log plot of Peak current and scan rate for NCV3-PC (h) Specific capacitance vs scan rate plot of CNF positive electrode (i) Specific capacitance vs current density plot of CNF positive electrode

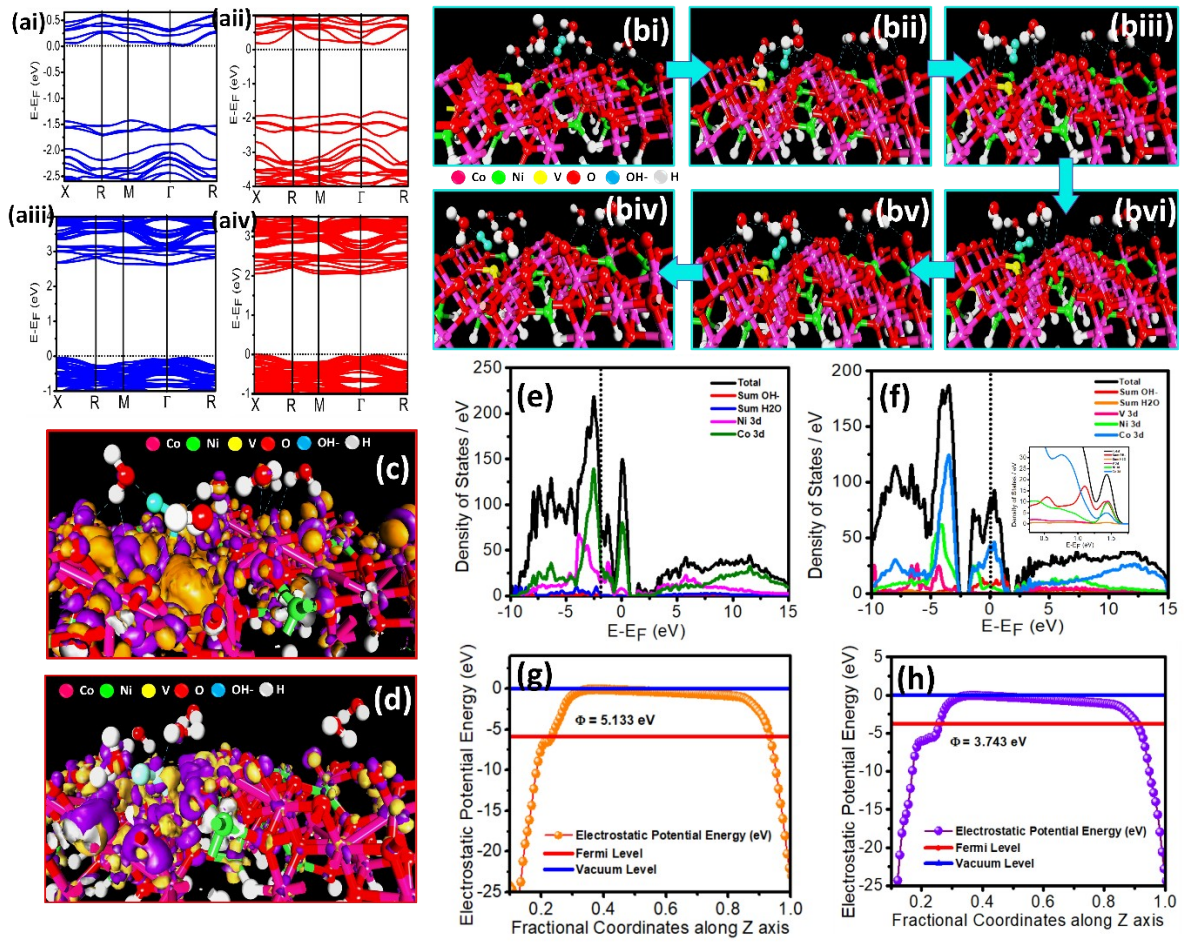

Fig S4 (a i-ii) Up and Down spin polarised band structure of V doped $NiCo_2O_4$ respectively (a iii-iv) Up and Down spin polarised band structure of pristine NiCo2O4 respectively (b i-iv) Diffusion path of hydrated OH- ion on the oxide slab surface (c) EDD isosurface of step 4 of Transition State (d) EDD isosurface of step 4 of Transition State (e) PDOS plot of step 5 of Transition State for pure $NiCo_2O_4$ (f) PDOS plot of step 4 of Transition State for V doped $NiCo_2O_4$ (g) Work function plot of pure $NiCo_2O_4$ (h) Work function plot of V doped $NiCo_2O_4$

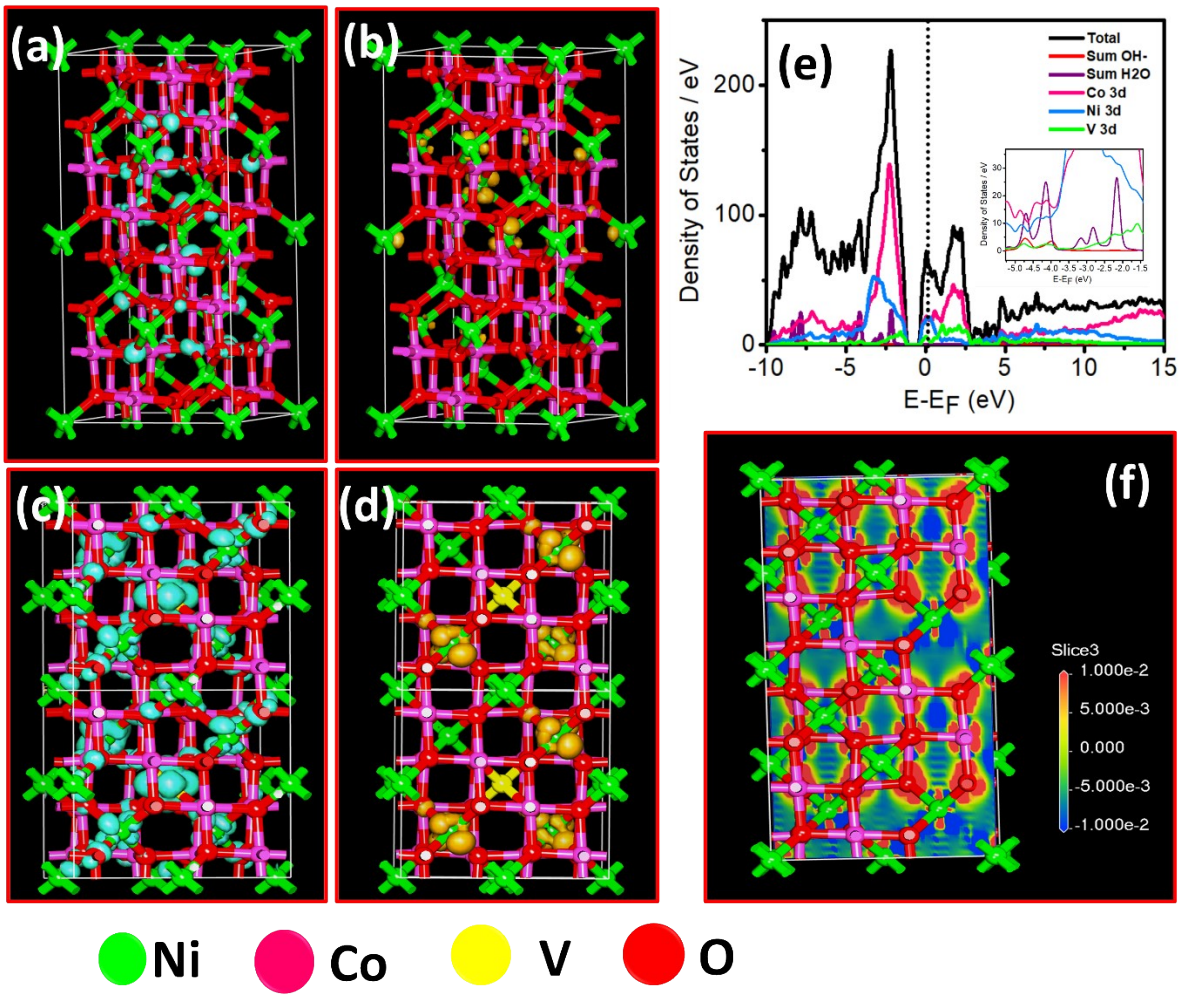

Fig S5 (a) HOMO plot of pure $NiCo_2O_4$ (b) LUMO plot of pure $NiCo_2O_4$ (c) HOMO plot of V doped $NiCo_2O_4$ (d) LUMO plot of V doped $NiCo_2O_4$ (e) PDOS plot of intermediate Step 5 (f) EDD plot of pure $NiCo_2O_4$

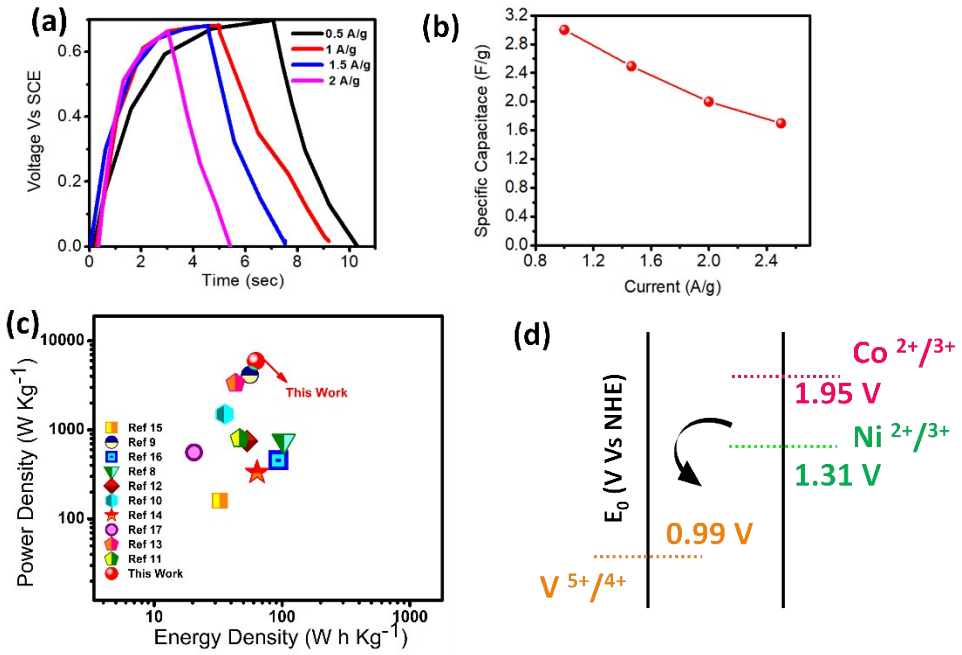

Fig S6 (a). GCD Plots of pristine carbon cloth (b) Specific capacitance vs current density plot of pristine carbon cloth (c) Ragone Plots of fabricated supercapacitor device compared with recent reports on similar $NiCo_2O_4$ based devices (d) Schematic diagram representing redox potentials of $Ni^{2+/3+}$ $Co^{2+/3+}$ and $V^{5+/4+}$ indicating feasibility of charge transfer.

References

1 I. Hussain, T. Mak and K. Zhang, *ACS Appl. Nano Mater.*, 2021, **4**, 129–141.

2 Y. Lin, X. Chen, Y. Tuo, Y. Pan and J. Zhang, *Journal of Energy Chemistry*, 2022, **70**, 27–35.

3 P. Bindu and S. Thomas, *Journal of Theoretical and Applied Physics*, 2014, **8**, 123–134.

4 D. Nath, F. Singh and R. Das, *Mater. Chem. Phys*, 2020, **239**, 122021.

5 X. Liu, C. Dong, X. Yuan, X. Wang, W. Dong and F. Huang, *RSC Adv.*, 2016, **6**, 29519–29523.

6 A. Patra, N. K., J. R. Jose, S. Sahoo, B. Chakraborty and C. S. Rout, *J. Mater. Chem. A Mater*, 2021, **9**, 25852–25891.

7 G. Yao, N. Zhang, Y. Zhang and T. Zhou, *Journal of Nanoparticle Research*, , DOI:10.1007/s11051-021-05158-9.

8 S. Wei, C. Wan, L. Zhang, X. Liu, W. Tian, J. Su and W. Cheng, *Chemical Engineering Journal*, 2022, **429**, 132242.

9 M. Chatterjee, S. Saha, S. Das and S. Kumar, *J. Alloys Compd*, 2020, **821**, 153503.

10 H. Rong, T. Chen, R. Shi, Y. Zhang and Z. Wang, *ACS Omega* 2018, 3, 5, 5634–5642.

11 T. Van Nguyen, L. T. Son, V. Van Thuy, V. D. Thao, M. Hatsukano, K. Higashimine, S. Maenosono, S. Chun and T. V. Thu, *Dalton Trans.*, 2020, **49**, 6718-67292020, 6718–6729.

12 W. Chu, Z. Shi, Y. Hou, D. Ma, X. Bai, Y. Gao and N. Yang, *ACS Appl. Mater. Interfaces* 2020, 12, 2, 2763–2772 , DOI:10.1021/acsami.9b13182.

13 G. P. Kamble, A. A. Kashale, A. S. Rasal and S. A. Mane, *RSC Adv.*, 2021, **11**, 3666-3672 2021, 3666–3672.

14 A. K. Yedluri and H. Kim, 2019, *RSC Adv.*, 2019, 9, 1115-1122 1115–1122.

15 C. Wang, G. Sui, D. Guo, J. Li, X. Ma and Y. Zhuang, *J Energy Storage*, 2022, **50**, 104280.

16 R. Nasser, X. Wang, A. Ben, G. Trabelsi, F. Homoud, H. Elhouichet and J. Song, *J. Energy Storage*, 2022, **52**, 104619.

17 X. Han, L. Song, J. Ding, L. Hu, C. Xu and Y. Wang, *Mater. Lett.*, 2020, **278**, 128400.

18 D. Adekoya, S. Qian, X. Gu, W. Wen, D. Li, J. Ma and S. Zhang, *DFT-Guided Design and Fabrication of Carbon-Nitride-Based Materials for Energy Storage Devices: A Review*, Springer Singapore, 2021, vol. 13.

19 Z. Zhou, P. Huo, L. Guo and O. V. Prezhdo, *Journal of Physical Chemistry C*, 2015, **119**, 26303–26310.

20 S. Lutfalla, V. Shapovalov and A. T. Bell, *J. Chem. Theory Comput.*, 2011, **7**, 2218–2223.

21 F. Opoku, K. Kuben Govender, C. G. C. E. van Sittert and P. Poomani Govender, *Phys. Chem. Chem. Phys.*, 2017, **19**, 28401-28413 .

22 N. Kishore, V. Nagarajan and R. Chandiramouli, *Journal of Nano- and Electronic Physics*, 2017, **9**, 3–6.

23 T. Wu, K. Zhu, C. Qin and K. Huang, *J. Mater. Chem. A Mater*, 2019, **7**, 5612–5620.

24 S. R. Sree, A. S. Shajahan, B. Chakraborty and C. S. Rout, *RSC Adv*, 2020, **10**, 31712–31719.

25 J. Liu, C. Zhang, L. Xu and S. Ju, *RSC Adv*, 2018, **8**, 17773–17785.

26 T. Zhang, H. Zhu, C. Guo, S. Cao, C. M. L. Wu, Z. Wang and X. Lu, *Catal Sci Technol*, 2020, **10**, 458–465.

27 Q. Tang and D. E. Jiang, *ACS Catal.*, 2016, **6**, 4953–4961.

28 L. Partanen, G. Murdachaew and K. Laasonen, *Journal of Physical Chemistry C*, 2018, **122**, 12892–12899.

29 A. Zagalskaya, I. Evazzade and V. Alexandrov, *ACS Energy Lett.*, 2021, **6**, 1124–1133.

30 Y. Abghoui and E. Skúlason, *Journal of Physical Chemistry C*, 2017, **121**, 24036–24045.

31 A. Chen, S. v. Nair, B. Miljkovic, H. E. Ruda and Z. Ji, *Journal of Electroanalytical Chemistry*, 2019, **855**, 113499.

32 Y. Peng, H. Hajiyani and R. Pentcheva, *ACS Catal*, 2021, **11**, 5601–5613.

33 M. Mousavi-Khoshdel, E. Targholi and M. J. Momeni, *Journal of Physical Chemistry C*, 2015, **119**, 26290–26295.

34 Q. Xu, G. M. Yang and W. T. Zheng, *Mater Today Commun*, , DOI:10.1016/j.mtcomm.2019.100772.

35 C. Song, J. Wang, Z. Meng, F. Hu and X. Jian, *ChemPhysChem*, 2018, **19**, 1579–1583.

36 Q. Xu, G. Yang, X. Fan and W. Zheng, *ACS Omega*, 2019, **4**, 13209–13217.

37 Q. Zhou, W. Ju, Y. Yong, Y. Liu and J. Li, *Comput Mater Sci*, 2021, **188**, 110131.

38 Q. Zhou, W. Ju, Y. Liu, J. Li and Q. Zhang, *Appl Surf Sci*, 2020, **510**, 145448.

39 H. Ullah, A. U. H. A. Shah, S. Bilal and K. Ayub, *Journal of Physical Chemistry C*, 2014, **118**, 17819–17830.